# Combined Tight-Binding and Numerical Electrodynamics Understanding of the STEM/EELS Magneto-optical Responses of Aromatic Plasmon-Supporting Metal Oligomers

Charles Cherqui,[‡] Nicholas W. Bigelow,[‡] Alex Vaschillo, Harrison Goldwyn, and David J. Masiello*

Department of Chemistry, University of Washington, Seattle, Washington 98195-1700, United States

ABSTRACT: The optical-frequency magnetic and electric properties of cyclic aromatic plasmon-supporting metal nanoparticle oligomers are explored through a combination of scanning transmission electron microscopy (STEM)/electron energy-loss spectroscopy (EELS) simulation and first-principles theory. A tight-binding-type model is introduced to explore the rich hybridization physics in these plasmonic systems and tested with full-wave numerical electrodynamics simulations of the STEM electron probe. Building from a microscopic electric model, connection is made at the macroscopic level between the hybridization of localized magnetic moments into delocalized magnetic plasmons of controllable magnetic order and the mixing of atomic p_z orbitals into delocalized π molecular orbitals of varying nodal structure spanning the molecule. It is found that the STEM electrons are uniquely capable of exciting all of the different hybridized eigenmodes of the nanoparticle assembly—including multipolar closed-loop ferromagnetic and antiferromagnetic plasmons, giant electric dipole resonances, and radial breathing modes—by raster scanning the beam to the appropriate position. Comparison to plane-wave light scattering and cathodoluminescence spectroscopy is made. The presented work provides a unified understanding of the complete plasmon eigenstructure of such oligomer systems as well as of the excitation conditions necessary to probe each mode.

KEYWORDS: magnetic plasmon resonances, electron energy-loss spectroscopy (EELS), scanning transmission electron microscopy (STEM), cathodoluminescence (CL) spectroscopy
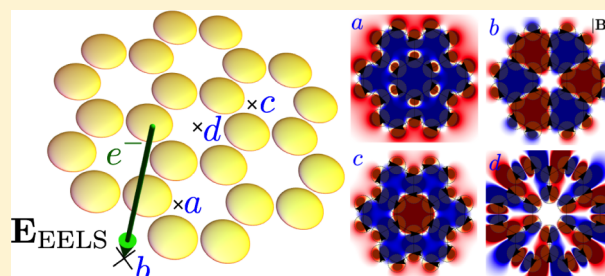
The magnetic permeability of the coinage metals is nearly that of vacuum in the visible part of the electromagnetic spectrum. However, when a localized surface plasmon resonance is excited on a metal nanoparticle, its electron density oscillation induces a small local magnetic field that is 90 degrees out of phase from its electric field. In spite of the relative weakness of this magnetic field, in 2005 Alù and Engheta[1] predicted that a sizable effective magnetic resonance could be generated within a collection of metal nanoparticles arranged on the corners of a rigid polygon due to the collective electric polarization of each particle.[2−4] This collective mode may hybridize in the "bonding" configuration (i.e., as electric dipoles organized head-to-tail around the polygon ring in a closed loop) to mimic a split-ring resonator[5] with multiple splits. When the system is driven resonantly at the frequency of its lowest lying eigenmode with either far-field plane-wave radiation[6,7] or in the near field with an electric or magnetic dipole,[8,9] a polarization current is set up that oscillates back and forth on each constituent nanoparticle. All together the nanoparticles conspire to localize their weak intrinsic magnetic fields constructively toward the ring center. This collective magnetic resonance has an effective magnetic moment—a so-called *magnetic plasmon*—that oscillates between north (counterclockwise) and south (clockwise) at optical frequencies. Assemblies of nanoparticles that support magnetic plasmon modes are defined to be magnetic metamaterials,

meaning that they possess anomalous magnetic properties beyond that of ordinary metals.

As multiple nanoparticle-based polygon assemblies are fused together into extended metal oligomers, the magnetic plasmon resonances of each ring unit cell mix and hybridize[10−12] just as electric plasmon resonances do,[13] forming new delocalized magnetic plasmons of varying magnetic character and nodal order. Evidence of this hybridization has already been predicted in near-linear chains of fused nanoparticle rings,[8,9] where the long-range propagation and interference of the maximally nodal antiferromagnetic plasmon was demonstrated. The existence of magnetic plasmon modes has also been demonstrated in metallodielectric nanoclusters,[14] where certain magnetic plasmon modes were transmuted to new ones through the addition of dielectric nanoparticles. Beyond the fundamental magnetic plasmon resonances described in these papers, the theory of plasmon hybridization further dictates the existence of delocalized plasmon resonances of varying magnetic and electric character and multipolar order. However, to date, no systematic and unifying first-principles understanding of the complete hybridized plasmon eigenstructure of such oligomer systems of arbitrary morphology has appeared in the literature. Nonetheless, magnetic plasmons have recently been the focus

of intense interest[7−12,14−43] due to their potential application in the design of metamaterials. The exploration of Fano effects based on the interference between magnetic and electric plasmon resonances has also attracted considerable investigation recently.[7,15,44] Beyond this literature, particular attention should be given to the work of van Aken and co-workers on the detection of toroidal modes in plasmonic nanocavities using energy-filtered transmission electron microscopy.[45,46] Babinet's principle dictates how the surface plasmon modes of an array of nanocavities are related to an array of nanoparticles of the same shape. Yet, this analogy has yet to be explored for these nanocavity arrays and the exotic magnetic resonances that they support.

It is a main purpose of this paper to construct a complete picture of both magnetic and electric plasmon hybridization across a family of experimentally accessible cyclic aromatic oligomer systems of arbitrary morphology and metallic composition. To illustrate the formalism in detail, we focus on the particular structures displayed in Figure 1. The
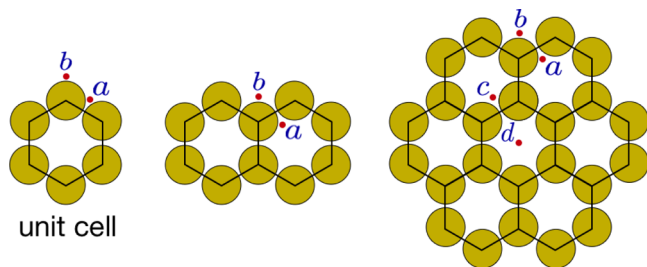
Figure 1. Planar cyclic assemblies of metal nanoparticles—so-called metal *oligomers*—arranged into a 1-mer (left), 2-mer (middle), and 6-mer (right), mimicking the aromatic molecules benzene, naphthalene, and coronene. Each system is constructed from the same hexagonal unit cell depicted in the left image. When resonantly driven at frequencies near the electric dipole plasmon resonance of an individual nanoparticle, the N-mer exhibits collective plasmon resonances of both electric and magnetic character that are delocalized across the entire assembly. The magnetic plasmon resonances of these N-mer systems are especially interesting, as they support optical-frequency magnetic moments of antiferromagnetic or ferromagnetic character of varying nodal order, all of which may be controllably excited by the electron beam of a STEM and detected in EELS. The particular aloof beam positions labeled a, b, c, and d (and their symmetric equivalents) will be investigated in the following.

geometries under consideration are composed of planar cyclic assemblies of metal nanoparticles arranged to mimic certain aromatic molecules.[47] This similarity allows us to exploit a corresponding microscopic electric and macroscopic magnetic tight-binding model. The tight-binding model for aromatic molecules is known as Hückel theory and is mathematically equivalent to the model of magnetic plasmon hybridization used in this paper.[48] Using these models, we find that such structures support a progression of hybridized multipolar magnetic plasmons of varying ferromagnetic and antiferromagnetic character as well as multipolar electric plasmons of giant dipole and radial breathing character. We further demonstrate through simulation that these hybridized plasmons can be individually excited by a scanning transmission electron microscope (STEM) and identified in electron energy-loss spectroscopy (EELS) and cathodoluminescence (CL) experiments. Such experiments are simulated with the full-wave electron-driven discrete-dipole approximation (e-DDA) code,

which numerically solves for the electrodynamics of a swift ion and its interaction with nearby metal surfaces.[49−53] The results are found to be in excellent agreement with those stemming from the tight-binding analysis.

The work presented here differs form previous studies of magnetic plasmons in several ways: earlier studies have focused on a few of the modes possible in single-ring systems[1,3,15] and in near-linear chains of coupled systems.[9] However, excitation of the complete eigenspectrum of collective magnetic and electric plasmon modes in aromatic nanoparticle oligomers by a STEM electron beam has not been explored previously. Consequently, their complete hybridization structure has not been fully appreciated. Larger and more extended systems exhibit even richer magnetic properties that could be useful in the development of magneto-inductive wave guides[54,55] and metamaterials.[56−59] The keV electrons generated within the STEM possess a high degree of spatial localization due to their sub-angstrom de Broglie wavelength, allowing one to specifically control the spatial location where energy is deposited into the system. This provides a mechanism for the systematic excitation of the entire plasmon eigenspectrum, which cannot be achieved with plane-wave excitation. It is the purpose of this paper to elucidate these diverse and controllable properties of extended cyclic magnetic-plasmon supporting nanostructures using analytic theory combined with STEM/EELS simulations.

■ TIGHT-BINDING MODELS OF INTERACTING LOCALIZED SURFACE PLASMON RESONANCES

Electric Tight-Binding Model. To model the electric plasmon resonances occurring in cyclic metal nanoparticle assemblies such as those displayed in Figure 1, we follow the coupled oscillator formalism of Lucas and co-workers.[60] This model treats the electric dipole response induced in the *i*th nanoparticle as a fictitious surface plasmon oscillator of mass m_{sp} and dipole moment $\mathbf{p}_i(\omega) \equiv \mathbf{p}(\mathbf{R}_i, \omega) = \boldsymbol{\alpha}(\omega) \cdot \mathbf{E}(\mathbf{R}_i, \omega)$ and is equivalent to the well-known hybridization theory[13] in the dipole limit. Particles located at positions $\mathbf{R}_i$ and $\mathbf{R}_j$ are coupled through their mutual electric dipole−electric dipole interaction, $-\mathbf{p}_i(t) \, \boldsymbol{\Lambda}^0_{ij} \, \mathbf{p}_j(t)$, where $\boldsymbol{\Lambda}^0_{ij} \equiv \boldsymbol{\Lambda}^0(\mathbf{R}_i, \mathbf{R}_j) = [3\hat{\mathbf{n}}_{ij}\hat{\mathbf{n}}_{ij} - \mathbf{1}_{ij}]/|R_i - R_j|^3$ is the near-field component of the standard electric dipole relay tensor evaluated in the quasi-static limit ($kd \ll 1$) and $\hat{\mathbf{n}}_{ij} \equiv (\mathbf{R}_i - \mathbf{R}_j)/|\mathbf{R}_i - \mathbf{R}_j|$. In the case where each particle is an isotropic metal nanosphere of radius d, its linear polarizability may be decomposed into the sum of two terms:

$$\boldsymbol{\alpha}(\omega) = \boldsymbol{\alpha}_C + \boldsymbol{\alpha}_{sp} \frac{\omega_{sp}^2}{\omega(\omega + i\gamma) - \omega_{sp}^2} \tag{1}$$

the first corresponding to the ionic core response and the second to the response of the electron gas confined to the surface of a sphere, giving it a resonant frequency of $\omega_{sp} = \Omega_{pl}/(\varepsilon_\infty + 2)^{1/2}$ in terms of the plasma frequency Ω_{pl}, a bulk dephasing rate of γ, and an infinite frequency relative permittivity ε_∞. Here, $\boldsymbol{\alpha}_C = d^3\mathbf{1}(\varepsilon_\infty - 1)/(\varepsilon_\infty + 2)$ and $\boldsymbol{\alpha}_{sp} = 3d^3\mathbf{1}/(\varepsilon_\infty + 2)$ are based upon the Drude model $\varepsilon(\omega) = \varepsilon_\infty - \Omega_{pl}^2/\omega(\omega + i\gamma)$ for the electronic response of the metal.

If we ignore the polarization of the core, we find that the time evolution of the dipole moment of the surface conduction electrons induced by an electric field **E** is described by
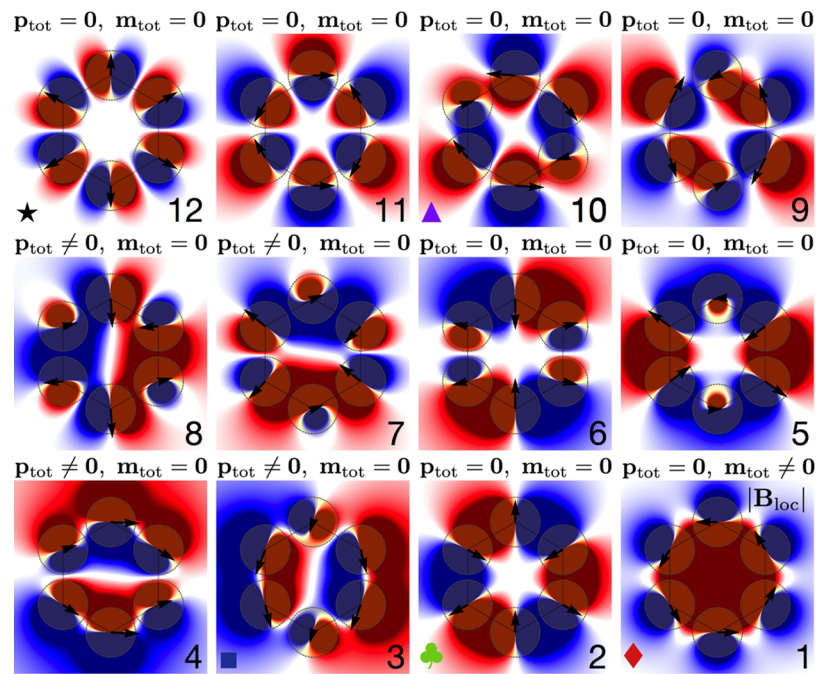
Figure 2. $|\mathbf{B}_{\text{loc}}|$ associated with each of the 12 tight-binding model eigenmodes of the 1-mer unit cell arranged in increasing energy order, labeled by ν = 1, ..., 12. Red (blue) represents a north (south) oriented magnetic dipole, while white represents the absence of a magnetic moment. The black arrows in each panel depict the electric dipole moments of the corresponding eigenmode. Circles are overlaid upon each dipole to indicate the locations of the underlying nanoparticles, although the latter are not explicitly included in the tight-binding model. The dipole moments of the ground state ($\nu = 1$) form a closed loop and act to localize their magnetic field into the center of the unit cell. They present no net electric dipole moment, but they collectively generate an effective magnetic moment. The latter is called a magnetic plasmon resonance.[1,3] In addition there are eigenmodes that correspond to giant electric dipoles ($\nu = 3,4$) and even a radial breathing mode ($\nu = 12$). Depending on the location of the STEM electron beam, each one of these features can be controllably excited and detected in EELS. The symbols appearing in each panel correspond to certain spectral positions in Figure 5. The net electric and magnetic moments $\mathbf{p}_{\text{tot}}$ and $\mathbf{m}_{\text{tot}}$ are overlaid above each eigenmode.

$$\mathbf{p}(\mathbf{R}, t) = \boldsymbol{\alpha}_{\text{sp}}\omega_{\text{sp}}^2 \int_{-\infty}^{t} dt' \frac{\sin\sqrt{\omega_{\text{sp}}^2 - (\gamma/2)^2}\,(t - t')}{\sqrt{\omega_{\text{sp}}^2 - (\gamma/2)^2}}$$
$$\times\, e^{-\gamma(t-t')/2}\mathbf{E}(\mathbf{R}, t') \tag{2}$$

which is the solution of the damped and driven harmonic oscillator $\ddot{\mathbf{p}}(\mathbf{R}, t) + \gamma\dot{\mathbf{p}}(\mathbf{R}, t) + \omega_{\text{sp}}^2\mathbf{p}(\mathbf{R}, t) = (-e^2/m_{\text{sp}})\mathbf{E}(\mathbf{R}, t)$. Neglecting damping, this equation can be derived from the classical Hamiltonian:

$$H_0 = \frac{\mathcal{P}^2}{2m_{\text{sp}}} + \frac{1}{2}m_{\text{sp}}\omega_{\text{sp}}^2\mathbf{u}^2 - (-e)\mathbf{u}\cdot\mathbf{E} \tag{3}$$

expressed in terms of its generalized coordinates for the displacement $\mathbf{u} = \mathbf{p}/(-e)$ and momentum $\mathcal{P}$ of the fictitious plasmon oscillator of mass $m_{\text{sp}} = e^2/\alpha_{\text{sp}}\omega_{\text{sp}}^2$, where α_{sp} is defined according to $\boldsymbol{\alpha}_{\text{sp}} = \alpha_{\text{sp}}\mathbf{1}$. Extension of eq 3 to an assembly of n metal nanoparticles interacting pairwise through the electric dipole−electric dipole potential energy $-\mathbf{p}_i(\omega)\,\boldsymbol{\Lambda}_{ij}^0\,\mathbf{p}_j(\omega)$ results in the total Hamiltonian.

$$H = \sum_i \left[\frac{\mathcal{P}_i^2}{2m_{\text{sp}}} + \frac{1}{2}m_{\text{sp}}\omega_{\text{sp}}^2\mathbf{u}_i^2\right] - \frac{e^2}{2}\sum_{ij}\mathbf{u}_i\cdot\boldsymbol{\Lambda}_{ij}^0\cdot\mathbf{u}_j \tag{4}$$

where the electric field appearing in H_0 is here generated by the $n - 1$ other nanoparticles according to $\mathbf{E}(\mathbf{R}_i, t) = \sum_{j\neq i}\boldsymbol{\Lambda}_{ij}^0 (-e)$ $\mathbf{u}_j(t)$. The first term in brackets is the sum of kinetic and potential energies for the localized surface plasmon resonance on each particle. The second term is the interaction energy of

the ith plasmon with the electric field produced by the jth plasmon.

It is convenient to recast eq 4 in terms of the dimensionless variables $\mathbf{Q}_i(t) = (m_{\text{sp}}\omega_{\text{sp}}/\hbar)^{1/2}\mathbf{u}_i(t)$ and $\boldsymbol{\Pi}_i(t) = \mathcal{P}_i(t)/\sqrt{\hbar m_{\text{sp}}\omega_{\text{sp}}}$, yielding

$$\frac{H}{\hbar\omega_{\text{sp}}} = \frac{1}{2}\sum_i [\boldsymbol{\Pi}_i^2 + \mathbf{Q}_i^2]$$
$$- \frac{1}{2}\sum_{ij} g_{ij}[3\mathbf{Q}_i\cdot\hat{\mathbf{n}}_{ij}\hat{\mathbf{n}}_{ij}\cdot\mathbf{Q}_j - \mathbf{Q}_i\cdot\mathbf{Q}_j] \tag{5}$$

with the dimensionless coupling constant $g_{ij} = \alpha_{\text{sp}}/d^3 r_{ij}^3 = (1/r_{ij}^3)(3/[\varepsilon_\infty + 2])$ and dimensionless distance between nanoparticles, $r_{ij} = |\mathbf{R}_i - \mathbf{R}_j|/d$. Restricting the nanoparticles to lie within a common plane and further restricting to nearest neighbor interactions removes the ij-dependence from r and g when the nanoparticles are positioned at the vertices of a regular polygon, such as is the case of the three N-mer assemblies displayed in Figure 1. This has the effect of simplifying the Hamiltonian even further by removing a direction of space (i.e., the direction normal to the plane) and simplifying the coupling constants. A route to quantization of the surface plasmon is now apparent by promoting the dynamical variables in eq 5 to operators and imposing upon them the commutation relations associated with boson statistics.[61,62] Interestingly, the coupling constant g is independent of the sphere radius and depends only on the ratio of the distance between the particles to their radius. This lack of dependence on the sphere radius is to be expected given that the quasi-static approximation is built into our tight-

binding model. Furthermore, since the dipole that represents the response of a nanosphere is located at the sphere center, there is a minimum value for r and in the limit that two spheres touch g has a maximum of $(1/2^3)(3/[\varepsilon_\infty + 2]) \neq \infty$.

It should be noted that this model neglects all quantum effects due to electron wave function spill out, electron tunneling between metal nanoparticles, and the discretization of energy levels as the particles become small enough to be classified as metal clusters. Such effects are important for nanoparticles separated at distances less than ~0.5 nm or for radii of only a few nanometers, imposing a lower bound on the validity of our model. Despite these limitations, it provides a reliable description of the energy eigenspectrum for the hybridized plasmon responses occurring within the N-mer nanoparticle assemblies discussed in this paper.

Diagonalization of the Hamiltonian in eq 5 for the planar 1-mer unit cell composed of six nanoparticles (see Figure 1, left panel) yields a set of 12 hybridized plasmon eigenmodes, $\{\mathbf{p}_i(t)\}_\nu$, labeled by $\nu = 1, ..., 12$. The spatial dependence of the magnetic field magnitude $|\mathbf{B}_\nu|$ associated with each through the curl of the vector potential $\mathbf{A}_\nu(\mathbf{x}, t) = \sum_{i=1}^{6}(-ik)\mathbf{p}_i^\nu(t) \exp(ik|\mathbf{x} - \mathbf{R}_i|)/|\mathbf{x} - \mathbf{R}_i|$ is displayed in Figure 2; here $k = \omega/c$ is the wave vector of light. The ground state is characterized as having electric dipole moments oriented tangent to the circle circumscribing the hexagon on which they lie. This head-to-tail or closed-loop arrangement of the dipoles allows for the concentration of the individual magnetic fields produced by each sphere toward the center of the unit cell, leading to a nontrivial focusing of the magnetic field into a *magnetic hot spot* with an effective magnetic moment. This is a well-known result, first proposed in 2005 by Alù and Engheta,[1] and is similar to how a split ring resonator operates.

When a collection of N unit cells is arranged into an N-mer, such as the 2-mer and 6-mer displayed in Figure 1, the spectrum of the Hamiltonian in eq 5 contains an even greater diversity of eigenmodes. Magnetic plasmons that are hybridizations of the effective magnetic moments of each unit cell arise as do fundamentally different plasmons of giant electric dipole and radial breathing character, among many others. Figure 3 and Figure 4 display the magnetic field magnitude, $|\mathbf{B}|$, corresponding to five eigenmodes of the 2-mer and the lowest lying nine eigenmodes of the 6-mer, computed from H in eq 5; the 2-mer has 20 and the 6-mer has 48 total hybridized eigenmodes. Some of the general features exposed by this model are as follows.

1. All ferromagnetic plasmon modes contain a net zero electric dipole moment and a net nonzero magnetic dipole moment.
2. The hybridized plasmon eigenenergies split with respect to the electric dipole response, $\hbar\omega_{sp}$, of a single nanoparticle, with the closed-loop magnetic modes all lying at the bottom, bounded from above by the collective giant dipole modes. All hybridized plasmon resonances of either electric or magnetic character reduce to that of the single nanoparticle's dipole plasmon in the limit where $g \rightarrow 0$.
3. The dynamics of the system is governed by nearest neighbor interactions, meaning that the local environment of each nanoparticle dominates the energetics of the collective assembly. Since all magnetic plasmon modes are composed of electric dipoles on adjacent particles oriented in a head-to-tail arrangement, they are
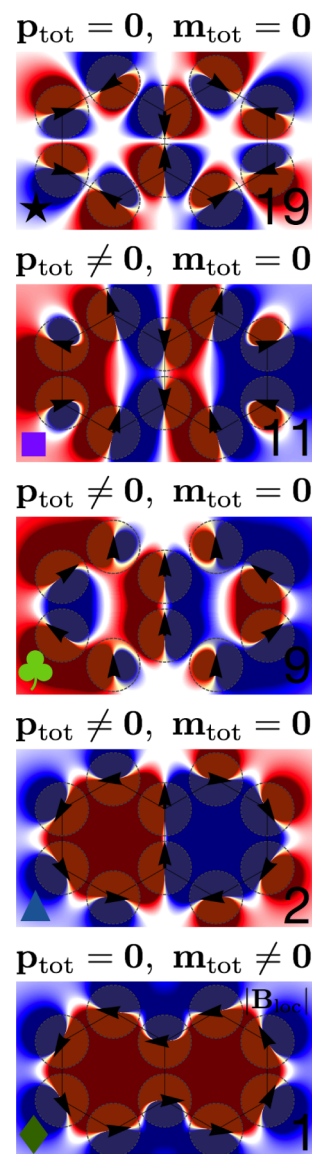
Figure 3. $|\mathbf{B}_{loc}|$ associated with five of the tight-binding model eigenmodes of the 2-mer arranged in increasing energy order, labeled by $\nu = 1, 2, 9, 11, 19$. Fifteen other eigenmodes also appear in the spectrum, which we do not display. With only two units cells, the 2-mer possesses only two hybridized magnetic plasmons. The ground state ($\nu = 1$) is ferromagnetic in character, with the magnetic moments on each unit cell pointing in the same direction. The opposite is true for the first excited state ($\nu = 2$), which is antiferromagnetic in character. A giant electric dipole plasmon ($\nu = 9$) also appears in the spectrum. Depending on the location of the STEM electron beam, each one of these features can be controllably excited and detected in EELS. The symbols appearing in each panel correspond to certain spectral positions in Figure 6. The net electric and magnetic moments $\mathbf{p}_{tot}$ and $\mathbf{m}_{tot}$ are overlaid above each eigenmode. Those eigenmodes of closed-loop magnetic character having $\mathbf{m}_{tot} = 0$ are antiferromagnetic, while those with $\mathbf{m}_{tot} \neq 0$ are ferromagnetic.

all nearly energetically degenerate. This means that choosing an excitation source with the right spectral and more importantly spatial behavior will be important when trying to excite a particular magnetic plasmon.

It is important to point out that because the electric Hamiltonian (eq 5) was derived within the quasi-static limit, it does not account for the total energy of the system whenever a
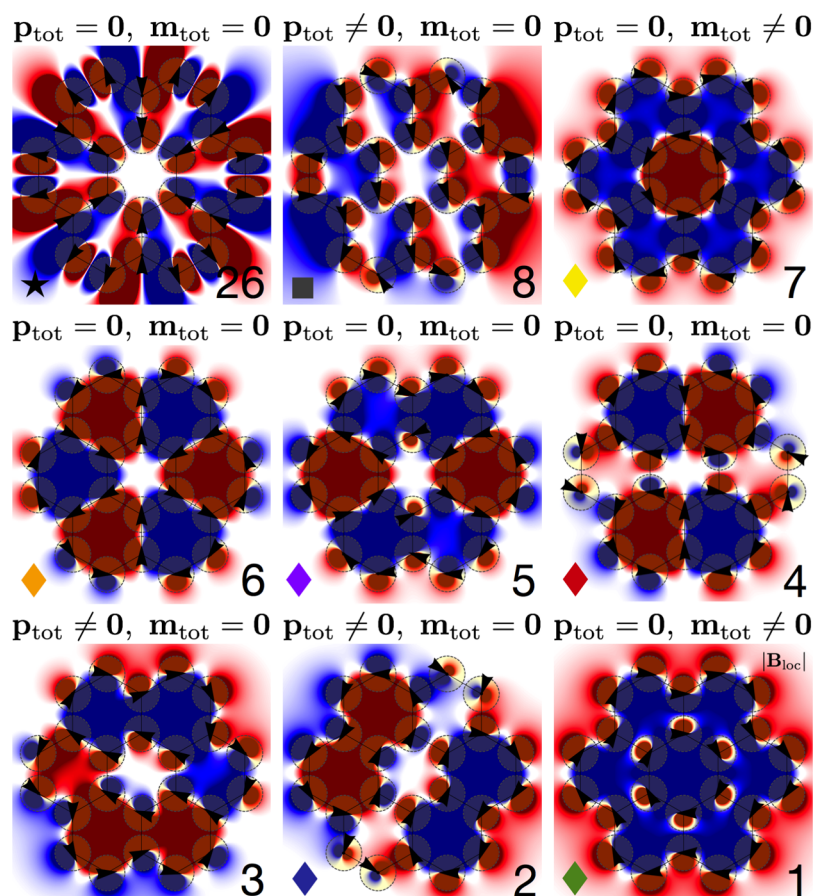
Figure 4. $|\mathbf{B}_{loc}|$ associated with nine of the tight-binding model eigenmodes of the 6-mer arranged in increasing energy order, labeled by $\nu = 1, ..., 8,$ 26. Thirty-nine additional eigenmodes also appear in the spectrum, which we do not display. With six unit cells, the 6-mer possesses seven hybridized magnetic plasmons. The ground state ($\nu = 1$) is ferromagnetic in character, with the magnetic moments on each unit cell pointing in the same direction. Beyond this appears a multipolar progression of hybridized magnetic plasmons ($\nu = 2-6$) of antiferromagnetic character and increasing angular nodal order. The ground state and the ferromagnetic excited state with one radial node ($\nu = 7$) bookend this collection of antiferromagnetic modes. A giant electric dipole ($\nu = 8$) and giant radial breathing mode ($\nu = 26$) also exist above all magnetic eigenmodes. The STEM electron beam can access each of these modes by raster scanning to the appropriate position. The symbols appearing in each panel correspond to certain spectral positions in Figure 7. The net electric and magnetic moments $\mathbf{p}_{tot}$ and $\mathbf{m}_{tot}$ are overlaid above each eigenmode. Those eigenmodes of closed-loop magnetic character having $\mathbf{m}_{tot} = \mathbf{0}$ are antiferromagnetic, while those with $\mathbf{m}_{tot} \neq \mathbf{0}$ are ferromagnetic.

nontrivial amount of energy is contained within the magnetic field. But this is precisely the case for all of the closed-loop magnetic modes of the N-mer. The consequences of this shortcoming are that the energy ordering of the magnetic modes among themselves is incorrect. For example in the case of the 2-mer, the antiferromagnetic plasmon (mode 2 in Figure 3) is predicted to have a lower energy than the ferromagnetic plasmon (mode 1 in Figure 3). However, as will be shown in the following, full-wave electrodynamics simulations reveal that the ferromagnetic mode is the ground state and the antiferromagnetic mode is the first excited state of the 2-mer. This inverse ordering should be expected if one adopts a circuit model in which in-phase current loops form the lowest energy configuration of the system.[11,63] Interestingly, while the specific energy ordering of the magnetic modes is incorrectly predicted by H, the specific polarization of individual nanoparticles for any given magnetic mode is nearly exactly predicted by the electric tight-binding formalism. This is the case for all N-mer systems. This breakdown in the model marks a transition from a system whose energetics are electrically dominated to a system where both electric and magnetic effects are important. To resolve this issue, several options exist, the most rigorous of

which is to solve Maxwell's equations, which we do in the following. Another approach is to coarse grain the N-mer into a collection of interacting magnetic moments, parametrized by their underlying electric interactions. The details of the latter will now be described.

Magnetic Tight-Binding Model. As kd becomes smaller, the electric near field extends to infinity and the magnetic field becomes negligible. It is, therefore, not surprising that the previous quasi-static electric tight-binding Hamiltonian is incomplete in its description of systems that store energy in the magnetic field. The metal oligomers under investigation in this paper are examples of systems where magnetic effects can be important. To properly understand their magnetic eigenmode structure, we will use the unique magnetic plasmon mode of the 1-mer to construct a coarse-grained magnetic tight-binding Hamiltonian.

The magnetic moment of the 1-mer unit cell's ground state may be well described as a magnetic dipole when the size of the unit cell is small in comparison to the wavelength of an interrogating photon of energy $\hbar\omega$. Even when this is not true, the dipole moment of a multipolar distribution of charge and current often describes the physics qualitatively correctly.

Neglecting damping, the magnetic dipole moment $\mathbf{m}$ associated with a collection of n electric dipoles p_i arranged in a closed loop with current density $\mathbf{J}(\mathbf{x}, t) = \sum_i \dot{\mathbf{p}}_i(t) \, \delta(x - \mathbf{R}_i)$ is

$$\mathbf{m}(\mathbf{R} = \mathbf{0}, t) = \frac{1}{2c} \int \mathbf{x} \times \mathbf{J}(\mathbf{x}, t) \, d^3x$$

$$= \frac{n\omega_M p R}{2c} \cos(\omega_M t)\hat{\mathbf{e}}_z, \qquad (6)$$

where $\mathbf{R} = \mathbf{0}$ is the location of the center of the unit cell, $\hbar\omega_M = \hbar\omega_{sp}((1 - 7g)/2)^{1/2}$ is the ground-state energy eigenvalue of eq 5, and $|\mathbf{R}_i| \equiv R$ and $|\mathbf{p}_i| \equiv p$ for $1 \leq i \leq n$. This magnetic dipole oscillates periodically in time at frequency ω_M and is characterized by the magnetic polarizability.

$$\boldsymbol{\alpha}_M(\omega) = \boldsymbol{\alpha}_{msp} \frac{\omega_M^2}{\omega(\omega + i\gamma_M) - \omega_M^2} \qquad (7)$$

where $|\boldsymbol{\alpha}_{msp}| \equiv \alpha_{msp} = n\alpha_{sp}/2$ and has a component only in the zz-direction. In this way, by excising all higher order eigenmodes from the eigenspectrum, the 1-mer unit cell is coarse-grained by $\mathbf{m}$.

In analogy with the procedure leading to eq 3, a tight-binding Hamiltonian for the unit cell can be defined that dictates the behavior of the single magnetic dipole $\mathbf{m}$ in a magnetic field $\mathbf{B}$. For a collection of N unit cells such as the 2-mer and 6-mer structures displayed in Figure 1, the effective magnetic dipole localized within each ring unit will hybridize with those on neighboring units through mutual magnetic dipole—magnetic dipole interactions of the form $-\mathbf{m}_i(t) \, \boldsymbol{\Lambda}_{ij}^0 \, \mathbf{m}_j(t)$, where $\mathbf{m}_i(\omega) \equiv \mathbf{m}(\mathbf{X}_i, \omega) = \boldsymbol{\alpha}_M(\omega) \cdot \mathbf{B}(\mathbf{X}_i, \omega)$. Restricting to nearest neighbors leads to the following dimensionless coarse-grained Hamiltonian for the N-mer:

$$\frac{H_M}{\hbar\omega_M} = \frac{1}{2} \sum_i \left[\pi_i^2 + q_i^2\right] - \frac{g_M}{2} {\sum_{ij}}' q_i q_j \qquad (8)$$

in analogy with eq 5, where the magnetic and electric coupling constants are connected by $g_M = g/n$ and where the prime on the sum denotes nearest neighbors. The symmetry of the system makes g_M the same for all i,j. Here $q_i(t) = (m_{msp}\omega_M/\hbar)^{1/2}|\mathbf{m}_i(t)|/(-e)$ and $\pi_i(t) = m_{msp}(|\dot{\mathbf{m}}_i(t)|/(-e))/(\hbar m_{msp}\omega_M)$ are the generalized dimensionless coordinates and momenta of a fictitious magnetic plasmon oscillator of mass $m_{msp} = e^2/\alpha_{msp}\omega_M^2$.

This is the magnetic plasmon equivalent of the Hückel Hamiltonian used in the description of the molecular orbitals of aromatic molecules. As the p_z atomic orbitals of an aromatic molecule hybridize into π molecular orbitals of varying nodal structure, so too do the magnetic dipole moments on each unit cell hybridize into collective magnetic plasmons that can be classified as ferromagnetic or antiferromagnetic in character. Like the Hückel Hamiltonian, which contains the coupling constants α and β expressing the strengths of the on-site and nearest neighbor interactions and which may be computed by accounting for the microscopic Coulombic interactions between electrons in the atomic orbitals, H_M contains coupling parameters that can be relayed back to the underlying microscopic physics of the electric dipole plasmons on each nanoparticle in the N-mer assembly. Once α_{sp} is known for a single particle, then all magnetic properties contained within H_M can be determined for a given assembly.

Diagonalization of the coarse-grained magnetic Hamiltonian H_M in eq 8 leads to an eigenspectrum comprising the hybridized magnetic dipole moments of an arbitrary planar N-mer. Because they are good approximations to the closed-loop hybridized magnetic eigenmodes of H, we do not display the eigenmodes of H_M but instead use their corresponding eigenenergies to properly reorder the magnetic eigenmodes of H. Figure 3 and Figure 4 display the hybridized plasmon resonances of the 2-mer and 6-mer composed of the same basic 1-mer unit cell described in Figure 1. The eigenmodes are computed from H in eq 5 and placed in order of their eigenenergies except for the closed-loop magnetic plasmons, which are reordered according to the corresponding eigenenergies of H_M. The 2-mer has only two hybridized magnetic plasmons; the ground state ($\nu = 1$) is ferromagnetic with the magnetic moments in each unit cell pointing in the same direction, while the opposite is true for the antiferromagnetic excited state ($\nu = 2$). The 6-mer possesses an even richer set of hybridized magnetic eigenmodes. The ground state and highest lying excited state ($\nu = 1$ and 7) are ferromagnets and bookend the magnetic part of the spectrum, while the five states in between ($\nu = 2-6$) are antiferromagnets of increasing nodal order. Effectively, we see a progression of modes that go from having a single well-defined magnetic moment at the center of mass of the N-mer to a fully antiferromagnetic character, the lowest mode being that with a single magnetic moment representing in-phase polarization currents in all unit cells and the highest energy antiferromagnetic mode being that with maximally out-of-phase polarization currents. The ferromagnetic ground state ($\nu = 1$) possesses a finite magnetic moment, as does the first ferromagnetic excited state ($\nu = 7$), while all antiferromagnetic modes have none. Because of this, the former modes are expected to have a signature in the system's CL response in addition to those modes supporting net electric dipole moments.

The analogy between this magnetic tight-binding model and Hückel theory is especially apparent in the eigenmodes of the 6-mer, with each 1-mer unit cell corresponding to a single carbon atom. However, there is one notable exception. Benzene has only six carbon atoms and six π molecular orbitals.[64] But the 6-mer has *seven* magnetic plasmon eigenmodes. Unlike in chemistry the central ring of the 6-mer behaves as a seventh unit cell (or as a seventh carbon atom). Because of this unique feature, the ferromagnetic modes 1 and 7 exist and have different energies. In fact there is no molecular analogue to the $\nu = 7$ mode of the 6-mer. Interestingly, modes 1−6 have the same degeneracy pattern as that of the Hückel description of benzene.[64] Full-wave electrodynamics simulation will also show this degeneracy pattern for all magnetic modes of the N-mer, although the magnitude of their splitting is quite small. The consequences of these facts will be discussed in the following.

■ FULL-WAVE ELECTRODYNAMICS SIMULATION AND DISCUSSION

We now investigate the behavior of these systems with full-wave e-DDA numerical electrodynamics simulations. The previous formalism has predicted a rich and diverse set of oligomer eigenmodes, but it is not clear *a priori* how well they approximate the solutions of Maxwell's equations. Nor is it clear what the necessary excitation conditions are to drive each mode. It is the purpose of this investigation to resolve these open questions by considering both optical and electron-beam driving sources. The eigenmode polarizations dictated by the tight-binding model are of critical importance in this analysis, as they will inform our choices of excitation source parameters
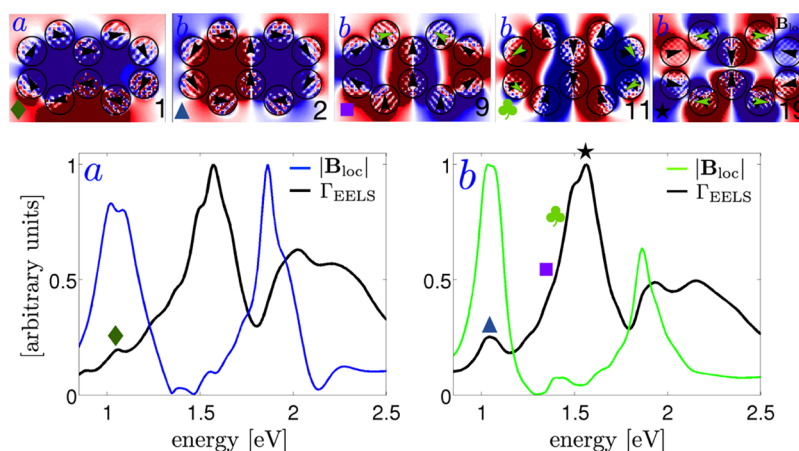
Figure 5. Normalized EEL probability Γ_{EELS} (black) and signed local magnetic field magnitude $|\mathbf{B}_{loc}|$ (blue/green) spectra (lower panels) of the 1-mer unit cell composed of 200 nm diameter by 15 nm thick gold nanodisks separated by 225 nm from center to adjacent center. The electron beam is positioned at the aloof locations a and b denoted in the left panel of Figure 1. All panels are computed from full-wave numerical electrodynamics simulations within the e-DDA. The spectrum of $|\mathbf{B}_{loc}|$ is evaluated by integrating the locally induced magnetic field magnitude inside the ring; red (blue) represents a north (south) oriented magnetic dipole, while white represents the absence of a magnetic moment. The upper panels display the spatial behavior of all of the energetically unique collective magnetic eigenmodes of the 1-mer that are excited at beam positions a and b. The corresponding electric tight-binding eigenmode, labeled by ν, is enumerated within each of the upper panels. The corresponding eigenmodes are overlaid as black arrows, with green arrows showing the deviation between model and simulation. Of particular importance is the ground-state eigenmode (upper left panel), where the electric dipole moments (black arrows) on each disk conspire to generate a magnetic field localized within the ring (♦). Such an eigenmode is referred to as a magnetic plasmon resonance.[1,3] Also shown is a primitive antiferromagnet (green clover), a giant electric dipole (■), and a pair of high-lying excited states (▲ and ★), one of radial breathing character (★). Modes of quadrupolar character also exist in the spectrum above ~1.7 eV (not explicitly shown), which are beyond the approximations built into the presented tight-binding model.
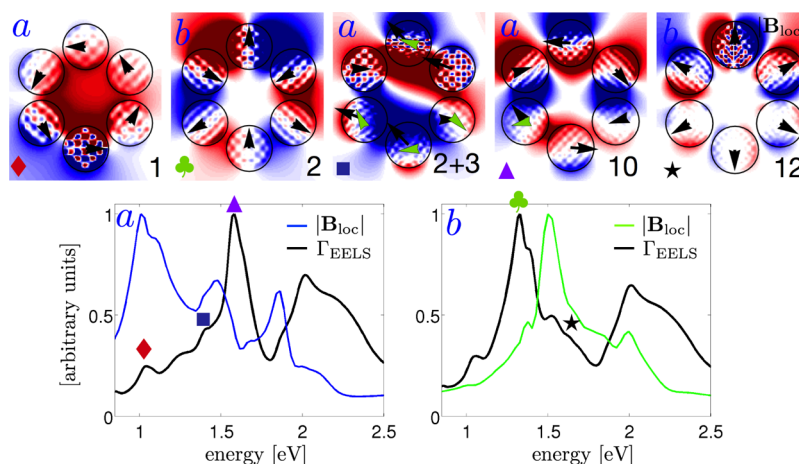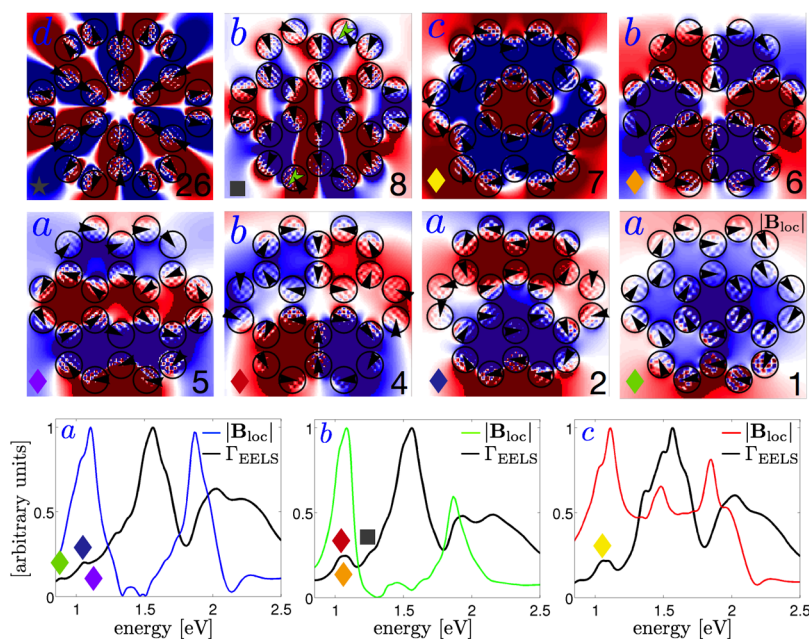

Figure 6. Normalized EEL probability Γ_{EELS} (solid black/red) and signed local magnetic field magnitude $|\mathbf{B}_{loc}|$ (dashed black/red) spectra (lower panel) of the 2-mer computed within the e-DDA. The electron beam is positioned at the aloof locations a and b denoted in the middle panel of Figure 1. The upper panels display the spatial behavior of a few of the 2-mer's collective eigenmodes that are excited at beam positions a and b. The corresponding tight-binding eigenmode is enumerated within each of the upper panels. Of particular importance is the ferromagnetic ground state (♦), where the magnetic moments in each unit cell point in the same direction. The first excited state is a closed-loop antiferromagnetic plasmon (▲), where the magnetic moments in each unit cell point in opposite directions. A giant electric dipole (■) and a radial breathing mode (★) also appear in the spectrum above both closed-loop magnetic plasmon modes.

such as the position of the electron beam relative to the target, thereby allowing us to drive specific modes of interest.

Rather than spheres we choose to employ nanodisks arranged on the corners of the hexagonal unit cell in Figure 1. None of the physics described previously is affected by this change. Each nanodisk is composed of gold,[65] has a 200 nm diameter, is 15 nm thick, and is separated by 225 nm (center to center) from the next adjacent particle in the lattice. For reference, the electric dipole plasmon of each individual nanodisk is located at 1.45 eV. All calculations employ a 100 keV electron beam to interrogate the system. Other nano-

particle shapes, sizes, separation distances, and material compositions that do not significantly differ from these parameters will only shift the collective plasmon resonances of the N-mer to other parts of the electromagnetic spectrum from the near UV through the visible to the near IR.

We first examine the 1-mer unit cell. Figure 5 displays the computed EEL probability Γ_{EELS} and local magnetic field magnitude $|\mathbf{B}_{loc}|$ spectra of the 1-mer at the aloof beam positions a and b shown in Figure 1. The electron-induced $|\mathbf{B}_{loc}|$ is computed by integrating the locally induced magnetic field magnitude inside the ring. The spectral location of the closed-

Figure 7. Normalized EEL probability Γ_{EELS} (black) and signed local magnetic field magnitude $|\mathbf{B}_{loc}|$ (blue/green/red) spectra (lower panel) of the 6-mer computed within the e-DDA. The electron beam is positioned at the aloof locations a, b, c, and d denoted in the right panel of Figure 1. The upper panels display the spatial behavior of a few of the 6-mer's collective eigenmodes that are excited at beam positions a, b, c, and d. The corresponding tight-binding eigenmode is enumerated within each of the upper panels. Of particular importance is the ferromagnetic ground state (blue, ♦), where the magnetic moments in all unit cells point in the same direction. The maximally nodal antiferromagnetic plasmon excited state (orange, ♦), where magnetic moments in each unit cell alternate in direction, is the highest lying magnetic plasmon of closed-loop character in the spectrum. Others of varying nodal order in both radial and angular directions appear in between these two modes. Also a giant dipole (■) appears in the spectrum above all closed-loop magnetic plasmon modes. The large peak in the EEL function near 1.5 eV is due, in part, to the excitation of the giant radial breathing mode of the 6-mer (★). For this reason we do not display the EEL spectrum at beam position d.

loop magnetic plasmon eigenmode can easily be gleaned by comparing the two spectra at position a. The upper panels show the spatial behavior of the $|\mathbf{B}_{loc}|$ associated with five of the collective plasmon eigenmodes of the 1-mer, all of which are predicted from and are enumerated in accordance with the tight-binding eigenstates labeled by ν. The ground state of the 1-mer is a closed-loop magnetic plasmon resonance (♦). Beyond that lies a primitive antiferromagnetic plasmon (clover), a giant electric dipole plasmon (■), and two high-lying states, one of which has the character of a radial breathing mode (★). These states, which are all accessible by the STEM electron beam, represent the complete set of energetically unique magnetic eigenmodes of the 1-mer. Other collective eigenmodes of quadrupolar (or higher multipolar) character might also appear in an experiment, but are not part of the presented tight-binding model. It is of course possible to extend the model to include such higher order multipolar effects.

When two unit cells are brought together into a 2-mer, the eigenmodes intrinsic to each rehybridize into an even richer set of eigenmodes spanning the dimer. Figure 6 displays the computed EEL probability Γ_{EELS} and local magnetic field magnitude $|\mathbf{B}_{loc}|$ spectra (lower panel) of the 2-mer at the aloof beam positions a and b shown in Figure 1. The electron-induced $|\mathbf{B}_{loc}|$ is computed by integrating the locally induced magnetic field magnitude within the closest ring unit adjacent to the electron beam. The upper panels show the spatial behavior of the $|\mathbf{B}_{loc}|$ associated with five of the collective plasmon eigenmodes of the 2-mer, all of which are predicted from and are enumerated in accordance with the tight-binding eigenstates labeled by ν. The ground state of the 2-mer is a closed-loop magnetic plasmon resonance that is characterized

by a colinear arrangement of the magnetic moments in each unit cell (♦). The first excited state, which is nearly degenerate with the previous, is also a closed-loop magnetic plasmon resonance, but has the magnetic moments in each unit cell pointing in opposite directions (▲). Together, they are the lowest energy ferromagnetic and antiferromagnetic plasmons of the 2-mer. Three other excited states of interest are identified, one of giant electric dipole character (clover) and the highest lying being an excited antiferromagnetic plasmon (★).

The hybridization patterns that occur on moving from the 1-mer to the 2-mer carryover to the 3-mer, 4-mer, and 5-mer (not shown) in a straightforward manner, independent of how the basic 1-mer unit cells within each are linked, i.e., either linearly or cyclically. Of particular note is the multipolar progression of magnetic plasmon resonances as the addition of another 1-mer introduces the possibility for another node in the magnetic plasmon density. However, a strikingly new behavior appears in the case where six 1-mers are arranged cyclically to form the 6-mer displayed in Figure 1. In this geometry the 6-mer is a rescaled version of the 1-mer, where each nanoparticle of the 1-mer is replaced by the 1-mer unit cell itself. The two structures share the same point group. This means that the 1-mer and 6-mer partially share a similar collection of eigenmodes, but on different length scales. For example, the ferromagnetic ground state ($\nu = 1$) of the 1-mer and 6-mer are equivalent. The primitive antiferromagnetic first excited state ($\nu = 2$) of the 1-mer is equivalent to the maximally nodal antiferromagnetic excited state ($\nu = 6$) of the 6-mer. The two primitive giant electric dipoles ($\nu = 3, 4$) of the 1-mer are equivalent to the giant electric dipoles hybridized across the 6-mer ($\nu = 8, 9$). The radial breathing mode ($\nu = 12$) of the 1-mer is equivalent

to the giant radial breathing mode of the 6-mer ($\nu = 26$; see Figure 7), etc.

Figure 7 displays the computed EEL probability Γ_{EELS} and local magnetic field magnitude $|\mathbf{B}_{loc}|$ spectra (lower panel) of the 6-mer at the aloof beam positions a, b, c, and d shown in Figure 1. The electron-induced $|\mathbf{B}_{loc}|$ is computed by averaging the local magnetic field induced inside the closest 1-mer ring unit to the electron beam. The upper panels show the spatial behavior of the $|\mathbf{B}_{loc}|$ associated with eight of the collective plasmon eigenmodes of the 6-mer, all of which are predicted from and are enumerated in accordance with the tight-binding eigenstates labeled by ν. The ground state of the 6-mer is a giant closed-loop ferromagnetic plasmon resonance that is characterized by a colinear arrangement of the magnetic moments in all six unit cells (green, ◆). It is important to point out that the central open ring within the 6-mer acts as an effective seventh unit cell and is involved in defining the magnetic moment of the ground state. In fact this central ring also participates in the $\nu = 7$ ferromagnetic eigenmode (yellow, ◆), which has one radial node separating it from the ground state, making it the first ferromagnetic excited state. This is in contrast to the aromatic benzene molecule, where all six of the π molecular orbitals are nearly zero in magnitude in the empty space within the six-membered carbon ring. In addition to these ferromagnetic plasmon modes the electron beam is also able to access all of the multipolar magnetic plasmon resonances of arbitrary nodal order in the angular direction ($\nu = 2, 4, 5, 6$). These modes are all of antiferromagnetic character since they have no net magnetic moment. For completeness we also show one of the giant electric dipoles (■) as well as a giant radial breathing mode (★). The latter appears most clearly at beam position d at 1.485 eV; however, since this resonance can also be seen at positions a, b, and c we do not show the EEL spectrum at position d. What we see developing here is that each class of hybridized magnetic and electric plasmon resonance of the N-mer (i.e., the antiferromagnet, ferromagnet, giant electric dipole, and radial electric breathing modes) has a ground state as well as a family of excited states of increasing nodal order.

Lastly, we discuss the differences between the STEM electron beam and the plane wave as an excitation source. In addition to this, we examine the signatures of the N-mer's various collective eigenmodes in cathodoluminescence spectroscopy. We have demonstrated that a subset of the full eigenspectrum of the N-mer can be excited in the STEM and detected in EELS by raster scanning to the appropriate beam position; other eigenmodes, which are not shown, are accessible at other locations. However, due to the polarization structure and delocalized nature of the plane wave in contrast to the localized evanescent electric field of the electron, the plane wave is incapable of accessing the entire eigenspectrum. When the plane wave's electric field is oriented in the plane of the N-mer, only those collective plasmon resonances of net electric dipolar character parallel to the polarization axis can be excited. Examples of this are the giant electric dipoles described previously. Alternatively, when the plane wave's magnetic field is oriented normal to the plane of the N-mer, a ring current is set up whose associated magnetic field acts to oppose the applied field in accordance with Lenz's law. This is precisely how the ground state magnetic plasmon of a single ring nanosystem was excited in ref 7. But this means that the magnetically polarized plane wave can excite only those magnetic plasmons of ferromagnetic character, because the

associated antiferromagnetic plasmons have no net magnetic moment and, therefore, are incapable of screening the applied magnetic field.

The CL response of the N-mer elucidates its collective magnetic and electric character further by indicating the net or total magnetic and electric dipole character of each eigenmode. An interesting consequence of the electron probe is that even plasmon eigenmodes that have no net electric dipole moment under plane-wave excitation can have a finite electric dipole character in electron spectroscopy due to the spatial localization of the electron beam when placed away from the target's center of symmetry. As a result, both ferromagnetic and antiferromagnetic plasmons can be detected in CL as well as EEL spectroscopies, although with weaker oscillator strength. Figure 8 compares the CL and EELS responses of the 2-mer, to
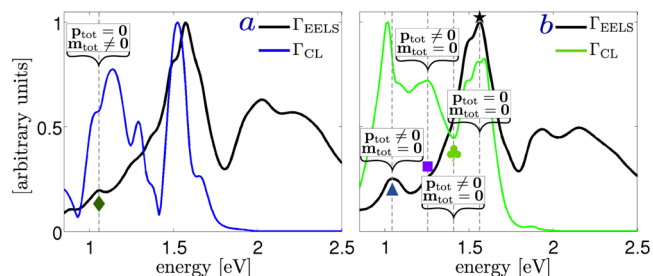
Figure 8. Normalized CL (blue/green) and EELS (black) responses of the same 2-mer system described previously in Figure 6, computed via the e-DDA. The electron beam is positioned at the aloof locations a and b denoted in the middle panel of Figure 1. All panels are computed from full-wave numerical electrodynamics simulations within the e-DDA. Because the CL spectrum encodes resonances of either net electric dipole $\mathbf{p}_{tot}$ or net magnetic dipole $\mathbf{m}_{tot}$ character (or neither), it is expected that the ferromagnetic ground state of the 2-mer (◆) will be visible in CL due to its finite magnetic dipole moment. The same is true for the antiferromagnetic excited state (▲) due its finite electric dipole moment. However, with $\mathbf{p}_{tot} = \mathbf{m}_{tot} = 0$ it is surprising to find the radial breathing mode (★) in the CL spectrum. This is due to the fact that the spatial localization of the electron beam excitation biases the system so that in the presence of loss a finite dipole moment arises even when the eigenmode itself has none. This is why eigenmodes of even formally zero electric and magnetic dipolar character can have a CL response. For comparison, the net moments $\mathbf{p}_{tot}$ and $\mathbf{m}_{tot}$ of the tight-binding eigenmodes themselves are overlaid upon the five resonances of interest.

illustrate the different information contained in each spectrum for the simplest nontrivial N-mer system. It is clear that both closed-loop magnetic modes (◆, ▲) of the 2-mer appear in the CL spectra, the ferromagnetic mode by having a finite magnetic dipole moment (◆) and the antiferromagnetic mode (▲) by having a finite electric dipole moment. Other nonmagnetic modes with a net electric dipole moment (■, clover) have CL responses as well. Interestingly, the $\nu = 19$ eigenmode (★) has no net electric or magnetic dipole, yet a strong response appears in the CL simulations at this loss energy due to the bias induced by the deep subwavelength localization of the electron beam. It is unclear if the small dip near 1.55 eV is the result of the lack of an electromagnetic dipole moment for mode 19 or if it is the result of other nearby mode structure dominating the response. In general, for these N-mer systems, the CL spectrum closely tracks the EELS spectrum in the region where the surface plasmon resonance of each nanodisk is well described by an electric dipole. At higher

energies the responses of the nanodisks begin to take on a quadrupolar character and the CL response drops to zero. Since the electric polarization of each nanodisk has no net dipole moment at these energies, the bias introduced by the position of the electron beam does not affect the CL spectrum.

CONCLUSION

Recent experimental advances in probing the magneto-optical properties of cyclic assemblies of plasmon-supporting metal nanoparticles linked into extended oligomers have provided impetus for a corresponding rigorous theoretical understanding of their rich structure and energetics. In this paper we present a first-principles theoretical description of the hybridization of the fundamental electric plasmons of each nanoparticle in the assembly into a family of delocalized oligomer plasmons based upon a combination of microscopic electric and macroscopic magnetic tight-binding models. Diagonalization of the corresponding Hamiltonian reveals a variety of hybridized surface plasmon resonances spanning the entire system, such as closed-loop magnetic plasmons of both ferromagnetic and antiferromagnetic character of varying multipolar order, giant electric dipole plasmons, and even plasmons that behave as giant radial breathing modes. The eigenmode spectrum is investigated in detail for three particular cyclic oligomers, the 1-mer, 2-mer, and 6-mer, and comparison is made to full-wave numerical simulations of their electron-driven responses. It found that the tight-binding formalism is in excellent agreement with the simulated EELS and, further, that all of the aforementioned modes can be systematically probed by the STEM electron beam and detected in EELS. Comparison is made to plane-wave excitation as well as to the CL response of the system. The work presented in this paper provides a rigorous and complete way to think about the collective electronic resonances of general oligomer systems of arbitrary morphology and material composition, advancing the design of future metamaterials with unprecedented magneto-optical properties.

METHODS

Electron Energy-Loss and Cathodoluminescence Simulations in e-DDA. The coupled-dipole[66] or DDA[67] approach is routinely used to study the response of metal nanoparticles subjected to optical-frequency radiation.[68] In our previous work we developed and numerically implemented the e-DDA[69,70] as a generalization of this approximation, incorporating the electron beam of a STEM in place of a plane-polarized electric field source as is common to the DDA. In the e-DDA the target is discretized into a finite collection of polarizable point dipoles $\mathbf{P}_j$, $1 \le j \le N$, each driven by the evanescent electric field

$$\mathbf{E}_{\text{electron}}(\mathbf{x}, \omega) = \frac{2e\omega}{v^2 \varepsilon \gamma} e^{i\omega z/v} \left[\frac{i}{\gamma} K_0 \left(\frac{\omega b}{v\gamma} \right) \hat{\mathbf{v}} - K_1 \left(\frac{\omega b}{v\gamma} \right) \hat{\mathbf{b}} \right]$$

(9)

of a passing swift electron as well as by the fully retarded electric-dipole field $\sum_{j \ne i}^{N} \mathbf{\Lambda}_{ij} \mathbf{P}_j$ generated by all other points; here $\mathbf{\Lambda}_{ij} = e^{ikr_{ij}}\{(1/r_{ij}^3 - ik/r_{ij}^2)[3\hat{\mathbf{n}}_{ij}\hat{\mathbf{n}}_{ij} - 1_{ij}] - k^2\hat{\mathbf{n}}_{ij} \times (\hat{\mathbf{n}}_{ij} \times)/r_{ij}\}$ is the standard dipole tensor that relays the electric field generated by a dipole at one point in space $\mathbf{x}_i$ to another $\mathbf{x}_j$ a distance $r_{ij}\hat{\mathbf{n}}_{ij} = |\mathbf{x}_i - \mathbf{x}_j|\hat{\mathbf{n}}_{ij}$ away. In this manner, the electron-induced responses of the system can be computed once each dipole is brought into self-consistency with all others at a certain value of the electron's loss energy, $\hbar\omega$. This is

accomplished through the iterative solution of the following equation:

$$\sum_{j=1}^{N} [\boldsymbol{\alpha}_{ii}^{-1}(\omega)\delta_{ij} - (1 - \delta_{ij})\mathbf{\Lambda}_{ij}] \cdot \mathbf{P}_j(\omega) = \mathbf{E}_{\text{electron}}(\mathbf{x}_i, \omega)$$

(10)

and depends upon the frequency-dependent linear polarizability $\boldsymbol{\alpha}_{ij}(\omega) \equiv \boldsymbol{\alpha}_{ii}(\varepsilon(\omega))\delta_{ij}$ of the target point i. The polarizability is related to the dielectric function through the lattice dispersion relation.[71] The electric field of the electron[72] in eq 9 depends upon the modified Bessel functions of the second kind K_0 and K_1, the Lorentz contraction factor $\gamma = 1/(1 - \varepsilon(v/c)^2)^{1/2}$, and the dielectric function ε of the background medium, which is taken to be vacuum in all presented calculations. The incident velocity $\mathbf{v} = v\hat{\mathbf{v}}$ of the electron is determined by its incident kinetic energy $m\gamma c^2 - mc^2$ and is oriented along the z axis. We choose the phase $e^{i\omega z/v} = 1$ at the z-height of the mass centroid of the target, which defines the plane of the impact parameter $\mathbf{b} = b\hat{\mathbf{b}}$, with $\mathbf{x} = (\mathbf{b}, z)$ that is perpendicular to the electron beam and that contains this point.

All target structures investigated via e-DDA simulations are excited by a 100 keV electron beam directed normal to plane of the N-mer; the corresponding velocity of the electrons in the beam is $0.55c$. Only aloof trajectories through a vacuum are considered in the simulations and the electron beam is never placed within one dipole spacing from the target, which is discretized at a dipole spacing of 5 nm; other values were tested to ensure that all spectra are converged at this value. Dielectric data from Johnson and Christy[65] are used for gold.

The most recent version of the e-DDA code[70] computes CL spectra and spatial maps in addition to EEL properties. The electron-induced response, $\mathbf{P}_j$, of the target is solved at each spatial position of the electron beam according to eq 10 as in the previous version of our code. However, for CL, at each spatial position of the beam and at each value of the loss energy, the induced electric field $\mathbf{E}_{\text{ind}}$ is computed according to

$$\mathbf{E}_{\text{ind}}(\mathbf{x}, \omega) = \sum_{j=1}^{N} \Lambda(\mathbf{x}, \mathbf{x}_j) \cdot \mathbf{P}_j(\omega)$$

(11)

at various points x in the far field. For the e-DDA-based CL calculations performed in this article, $\mathbf{E}_{\text{ind}}$ is computed on an angular grid of points spanning the surface of a distant sphere of radius 5 μm, with 75 points in θ and 75 points in φ. In this way, either the differential CL response $d\Gamma_{\text{CL}}/d\Omega$ or, by quadratured solid-angle integration, the total CL response Γ_{CL} may be computed.

AUTHOR INFORMATION

Corresponding Author
*E-mail: masiello@chem.washington.edu.

Author Contributions
‡C. Cherqui and N. W. Bigelow contributed equally to this work.

Notes
The authors declare no competing financial interest.

Thakkar from the University of Washington as well as Prof. John F. Stanton from the University of Texas at Austin for fruitful discussions.

■ REFERENCES

(1) Alù, A.; Engheta, N. Achieving transparency with plasmonic and metamaterial coatings. *Phys. Rev. E* **2005**, *72*, 016623.

(2) Alù, A.; Salandrino, A.; Engheta, N. Negative effective permeability and left-handed materials at optical frequencies. *Opt. Express* **2006**, *14*, 1557−1567.

(3) Alú, A.; Engheta, N. The quest for magnetic plasmons at optical frequencies. *Opt. Express* **2009**, *17*, 5723−5730.

(4) Alù, A.; Engheta, N. Dynamical theory of artificial optical magnetism produced by rings of plasmonic nanoparticles. *Phys. Rev. B* **2008**, *78*, 085112.

(5) Pendry, J.; Holden, A.; Stewart, W.; Youngs, I. Extremely low frequency plasmons in metallic mesostructures. *Phys. Rev. Lett.* **1996**, *76*, 4773.

(6) Fan, J. A.; Wu, C.; Bao, K.; Bao, J.; Bardhan, R.; Halas, N. J.; Manoharan, V. N.; Nordlander, P.; Shvets, G.; Capasso, F. Self-assembled plasmonic nanoparticle clusters. *Science* **2010**, *328*, 1135−1138.

(7) Sheikholeslami, S. N.; García-Etxarri, A.; Dionne, J. A. Controlling the interplay of electric and magnetic modes via Fano-like plasmon resonances. *Nano Lett.* **2011**, *11*, 3927−3934.

(8) Liu, N.; Mukherjee, S.; Bao, K.; Brown, L. V.; Dorfmüller, J.; Nordlander, P.; Halas, N. J. Magnetic plasmon formation and propagation in artificial aromatic molecules. *Nano Lett.* **2012**, *12*, 364−369.

(9) Liu, N.; Mukherjee, S.; Bao, K.; Li, Y.; Brown, L. V.; Nordlander, P.; Halas, N. J. Manipulating magnetic plasmon propagation in metallic nanocluster networks. *ACS Nano* **2012**, *6*, 5482−5488.

(10) Liu, H.; Genov, D.; Wu, D.; Liu, Y.; Steele, J.; Sun, C.; Zhu, S.; Zhang, X. Magnetic plasmon propagation along a chain of connected subwavelength resonators at infrared frequencies. *Phys. Rev. Lett.* **2006**, *97*, 243902.

(11) Liu, H.; Genov, D.; Wu, D.; Liu, Y.; Liu, Z.; Sun, C.; Zhu, S.; Zhang, X. Magnetic plasmon hybridization and optical activity at optical frequencies in metallic nanostructures. *Phys. Rev. B* **2007**, *76*, 073101.

(12) Zhu, D.; Bosman, M.; Yang, J. K. W. A circuit model for plasmonic resonators. *Opt. Express* **2014**, *22*, 9809−9819.

(13) Prodan, E.; Radloff, C.; Halas, N. J.; Nordlander, P. A hybridization mdoel for the plasmon response of complex nanostructures. *Science* **2003**, *302*, 419−422.

(14) Wen, F.; Ye, J.; Liu, N.; Van Dorpe, P.; Nordlander, P.; Halas, N. J. Plasmon transmutation: inducing new modes in nanoclusters by adding dielectric nanoparticles. *Nano Lett.* **2012**, *12*, 5020−5026.

(15) Campione, S.; Guclu, C.; Ragan, R.; Capolino, F. Enhanced magnetic and electric fields via Fano resonances in metasurfaces of circular clusters of plasmonic nanoparticles. *ACS Photonics* **2014**, *1*, 254−260.

(16) Sheikholeslami, S. N.; Alaeian, H.; Koh, A. L.; Dionne, J. A. A metafluid exhibiting strong optical magnetism. *Nano Lett.* **2013**, *13*, 4137−4141.

(17) Wang, J.; Fan, C.; He, J.; Ding, P.; Liang, E.; Xue, Q. Double Fano resonances due to interplay of electric and magnetic plasmon modes in planar plasmonic structure with high sensing sensitivity. *Opt. Express* **2013**, *21*, 2236−2244.

(18) Alaeian, H.; Dionne, J. A. Plasmon nanoparticle superlattices as optical-frequency magnetic metamaterials. *Opt. Express* **2012**, *20*, 15781−15796.

(19) Zhu, Z.; Guo, C.; Liu, K.; Ye, W.; Yuan, X.; Yang, B.; Ma, T. Metallic nanofilm half-wave plate based on magnetic plasmon resonance. *Opt. Lett.* **2012**, *37*, 698−700.

(20) Miroshnichenko, A. E.; Luk'yanchuk, B.; Maier, S. A.; Kivshar, Y. S. Optically induced interaction of magnetic moments in hybrid metamaterials. *ACS Nano* **2011**, *6*, 837−842.

(21) Tang, C.; Zhan, P.; Cao, Z.; Pan, J.; Chen, Z.; Wang, Z. Magnetic field enhancement at optical frequencies through diffraction coupling of magnetic plasmon resonances in metamaterials. *Phys. Rev. B* **2011**, *83*, 041402.

(22) Cao, J.; Liu, H.; Li, T.; Wang, S.; Dong, Z.; Zhu, S. High sensing properties of magnetic plasmon resonance in the double-rod and tri-rod structures. *Appl. Phys. Lett.* **2010**, *97*, 071905.

(23) Li, K. H.; Yellen, B. B. Magnetically tunable self-assembly of colloidal rings. *Appl. Phys. Lett.* **2010**, *97*, 083105.

(24) Lu, Y.; Xu, H.; Rhee, J. Y.; Jang, W. H.; Ham, B. S.; Lee, Y. Magnetic plasmon resonance: underlying route to plasmonic electromagnetically induced transparency in metamaterials. *Phys. Rev. B* **2010**, *82*, 195112.

(25) Wang, S.; Zhu, Z.; Cao, J.; Li, T.; Liu, H.; Zhu, S.; Zhang, X. The gain effect in a magnetic plasmon waveguide. *Appl. Phys. Lett.* **2010**, *96*, 113103.

(26) Wheeler, M. S.; Aitchison, J. S.; Mojahedi, M. Coupled magnetic dipole resonances in sub-wavelength dielectric particle clusters. *J. Opt. Soc. Am. B* **2010**, *27*, 1083−1091.

(27) Zhu, C.; Liu, H.; Wang, S.; Li, T.; Cao, J.; Zheng, Y.; Li, L.; Wang, Y.; Zhu, S.; Zhang, X. Electric and magnetic excitation of coherent magnetic plasmon waves in a one-dimensional meta-chain. *Opt. Express* **2010**, *18*, 26268−26273.

(28) Hao, Z.; Chubukov, A. Resonance peak in neutron scattering experiments on the cuprates revisited: The case of exciton versus *p*-resonance and magnetic plasmon. *Phys. Rev. B* **2009**, *79*, 224513.

(29) Li, T.; Ye, R.; Li, C.; Liu, H.; Wang, S.; Cao, J.; Zhu, S.; Zhang, X. Structural-configured magnetic plasmon bands in connected ring chains. *Opt. Express* **2009**, *17*, 11486−11494.

(30) Liu, H.; Liu, Y.; Li, T.; Wang, S.; Zhu, S.; Zhang, X. Coupled magnetic plasmons in metamaterials. *Phys. Status Solidi (B)* **2009**, *246*, 1397−1406.

(31) Liu, H.; Li, T.; Wang, Q.; Zhu, Z.; Wang, S.; Li, J.; Zhu, S.; Zhu, Y.; Zhang, X. Extraordinary optical transmission induced by excitation of a magnetic plasmon propagation mode in a diatomic chain of slit-hole resonators. *Phys. Rev. B* **2009**, *79*, 024304.

(32) Zhu, Z.; Liu, H.; Wang, S.; Li, T.; Cao, J.; Ye, W.; Yuan, X.; Zhu, S. Optically pumped nanolaser based on two magnetic plasmon resonance modes. *Appl. Phys. Lett.* **2009**, *94*, 103106.

(33) Li, T.; Wang, S.-M.; Liu, H.; Li, J.-Q.; Wang, F.-M.; Zhu, S.-N.; Zhang, X. Dispersion of magnetic plasmon polaritons in perforated trilayer metamaterials. *J. Appl. Phys.* **2008**, *103*, 023104.

(34) Li, T.; Liu, H.; Li, T.; Wang, S.; Wang, F.; Wu, R.; Chen, P.; Zhu, S.; Zhang, X. Magnetic resonance hybridization and optical activity of microwaves in a chiral metamaterial. *Appl. Phys. Lett.* **2008**, *92*, 131111.

(35) Liu, N.; Fu, L.; Kaiser, S.; Schweizer, H.; Giessen, H. Plasmonic building blocks for magnetic molecules in three-dimensional optical metamaterials. *Adv. Mater.* **2008**, *20*, 3859−3865.

(36) Lu, D.; Liu, H.; Li, T.; Wang, S.; Wang, F.; Zhu, S.; Zhang, X. Creation of a magnetic plasmon polariton through strong coupling between an artificial magnetic atom and the defect state in a defective multilayer microcavity. *Phys. Rev. B* **2008**, *77*, 214302.

(37) Wang, S.; Li, T.; Liu, H.; Wang, F.; Zhu, S.; Zhang, X. Magnetic plasmon modes in periodic chains of nanosandwiches. *Opt. Express* **2008**, *16*, 3560−3565.

(38) Li, T.; Li, J.-Q.; Wang, F.-M.; Wang, Q.-J.; Liu, H.; Zhu, S.-N.; Zhu, Y.-Y. Exploring magnetic plasmon polaritons in optical transmission through hole arrays perforated in trilayer structures. *Appl. Phys. Lett.* **2007**, *90*, 251112.

(39) Pakizeh, T.; Abrishamian, M.; Granpayeh, N.; Dmitriev, A.; Käll, M. Magnetic-field enhancement in gold nanosandwiches. *Opt. Express* **2006**, *14*, 8240−8246.

(40) Sarychev, A. K.; Shvets, G.; Shalaev, V. M. Magnetic plasmon resonance. *Phys. Rev. E* **2006**, *73*, 036609.

(41) Sarychev, A. K.; Shalaev, V. M. Magnetic resonance in metal nanoantennas. *Proc. SPIE* **2004**, *5508*, 129.

(42) Yang, J.; Rahmani, M.; Teng, J.; Hong, M. Magnetic-electric interference in metal-dielectric-metal oligomers: generation of

magneto-electric Fano resonance. *Opt. Mater. Express* **2012**, *2*, 1407−1415.

(43) Wu, P. C.; Chen, W. T.; Yang, K.-Y.; Hsiao, C. T.; Sun, G.; Liu, A. Q.; Zheludev, N. I.; Tsai, D. P. Magnetic plasmon induced transparency in three-dimensional metamolecules. *Nanophotonics* **2012**, *1*, 131−138.

(44) Nazir, A.; Panaro, S.; Proietti Zaccaria, R.; Liberale, C.; de Angelis, F.; Toma, A. Fano coil-type resonance for magnetic hot-spot generation. *Nano Lett.* **2014**, *14*, 3166−3171.

(45) Ögüt, B.; Talebi, N.; Vogelgesang, R.; Sigle, W.; van Aken, P. A. Toroidal plasmonic eigenmodes in oligomer nanocavities for the visible. *Nano Lett.* **2012**, *12*, 5239−5244.

(46) Talebi, N.; Ögüt, B.; Sigle, W.; Vogelgesang, R.; van Aken, P. A. On the symmetry and topology of plasmonic eigenmodes in heptamer and hexamer nanocavities. *Appl. Phys. A: Mater. Sci. Processes* **2014**, 1−8.

(47) Guerrero-Martnez, A.; Grzelczak, M.; Liz-Marzán, L. M. Molecular thinking for nanoplasmonic design. *ACS Nano* **2012**, *6*, 3655−3662.

(48) Economou, E. N. *Green's Functions in Quantum Physics*; Springer: Berlin, 1984; Vol. 3.

(49) García de Abajo, F. J.; Howie, A. Retarded field calculation of electron energy loss in inhomogeneous dielectrics. *Phys. Rev. B* **2002**, *65*, 115418.

(50) Echenique, P.; Howie, A.; Wheatley, D. Excitation of dielectric spheres by external electron beams. *Philos. Mag. B* **1987**, *56*, 335−349.

(51) Crowell, J.; Ritchie, R. Radiative decay of Coulomb-stimulated plasmons in spheres. *Phys. Rev.* **1968**, *172*, 436−440.

(52) Lucas, A.; Sunjic, M. Fast-electron spectroscopy of surface excitations. *Phys. Rev. Lett.* **1971**, *26*, 229−232.

(53) García de Abajo, F. J. Optical excitations in electron microscopy. *Rev. Mod. Phys.* **2010**, *82*, 209.

(54) Lipworth, G.; Ensworth, J.; Seetharam, K.; Huang, D.; Lee, J. S.; Schmalenberg, P.; Nomura, T.; Reynolds, M. S.; Smith, D. R.; Urzhumov, Y. Magnetic Metamaterial Superlens for Increased Range Wireless Power Transfer. *Sci. Rep.* **2014**, *4*.

(55) Palma-Chilla, L.; Flores, J.; Vega-Jorquera, P. Connections between the dissipated energy of right-handed and left-handed systems: electric and magnetic origin. *J. Electromagn. Waves Appl.* **2014**, *28*, 129−137.

(56) Zhu, W. M.; Liu, A. Q.; Zhang, X. M.; Tsai, D. P.; Bourouina, T.; Teng, J. H.; Zhang, X. H.; Guo, H. C.; Tanoto, H.; Mei, T.; et al. Switchable magnetic metamaterials using micromachining processes. *Adv. Mater.* **2011**, *23*, 1792−1796.

(57) Klein, M. W.; Enkrich, C.; Wegener, M.; Linden, S. Second-harmonic generation from magnetic metamaterials. *Science* **2006**, *313*, 502−504.

(58) Enkrich, C.; Wegener, M.; Linden, S.; Burger, S.; Zschiedrich, L.; Schmidt, F.; Zhou, J.; Koschny, T.; Soukoulis, C. Magnetic metamaterials at telecommunication and visible frequencies. *Phys. Rev. Lett.* **2005**, *95*, 203901.

(59) O'Brien, S.; McPeake, D.; Ramakrishna, S.; Pendry, J. Near-infrared photonic band gaps and nonlinear effects in negative magnetic metamaterials. *Phys. Rev. B* **2004**, *69*, 241101.

(60) Ausloos, M.; Clippe, P.; Lucas, A. A. Infrared active modes in large clusters of spheres. *Phys. Rev. B* **1978**, *18*, 7176−7185.

(61) Fujii, G.; Fukuda, D.; Inoue, S. Direct observation of bosonic quantum interference of surface plasmon polaritons using photon-number-resolving detectors. *Phys. Rev. B* **2014**, *90*, 085430.

(62) Fakonas, J. S.; Lee, H.; Kelaita, Y. A.; Atwater, H. A. Two-plasmon quantum interference. *Nat. Photonics* **2014**, *8*, 317−320.

(63) Willingham, B.; Link, S. A Kirchhoff solution to plasmon hybridization. *Appl. Phys. B: Laser Opt.* **2013**, *113*, 519−525.

(64) Atkins, P. W. *Physical Chemistry*, 6th ed.; Oxford University Press, 1998.

(65) Johnson, P. B.; Christy, R. W. Optical Constants of the Noble Metals. *Phys. Rev. B* **1972**, *6*, 4370.

(66) Purcell, E. M.; Pennypacker, C. R. Scattering and absorption of light by nonspherical dielectric grains. *Astrophys. J.* **1973**, *186*, 705.

(67) Draine, B. T.; Flatau, P. J. Discrete-dipole approximation for scattering calculations. *J. Opt. Soc. Am. A* **1994**, *11*, 1491.

(68) Kelly, K. L.; Coronado, E.; Zhao, L. L.; Schatz, G. C. The optical properties of metal nanoparticles: the influence of size, shape, and dielectric environment. *J. Phys. Chem. B* **2003**, *107*, 668.

(69) Bigelow, N. W.; Vaschillo, A.; Iberi, V.; Camden, J. P.; Masiello, D. J. Characterization of the electron- and photon-driven plasmonic excitations of metal nanorods. *ACS Nano* **2012**, *6*, 7497−7504.

(70) Masiello Group Website, Theory of Molecular Plasmonics and Optics on the Nanoscale. http://faculty.washington.edu/masiello.

(71) Draine, B. T.; Goodman, J. Beyond Clausius-Mossotti: wave propagation on a polarizable point lattice and the discrete dipole approximation. *Astrophys. J.* **1993**, *405*, 685.

(72) Jackson, J. D. *Classical Electrodynamics*, 3rd ed.; J. Wiley & Sons: New York, 1999.